Observation of gapless nodal-line states in NdSbTe

Sabin Regmi [ORCID],[1] Robert Smith,[1] Anup Pradhan Sakhya,[1] Milo Sprague,[1] Mazharul Islam Mondal [ORCID],[1] Iftakhar Bin Elius [ORCID],[1] Nathan Valadez,[1] Andrzej Ptok [ORCID],[2] Dariusz Kaczorowski [ORCID],[3] and Madhab Neupane [ORCID][1,*]

[1]*Department of Physics, University of Central Florida, Orlando, Florida 32816, USA*
[2]*Institute of Nuclear Physics, Polish Academy of Sciences, W. E. Radzikowskiego 152, PL-31342 Kraków, Poland*
[3]*Institute of Low Temperature and Structure Research, Polish Academy of Sciences, Okólna 2, PL-50-422 Wrocław, Poland*

Lanthanide (*Ln*)-based systems in ZrSiS-type nodal-line semimetals have been subjects of research investigations as grounds for studying the interplay of topology with possible magnetic ordering and electronic correlations that may originate from the presence of *Ln* $4f$ electrons. In this study, we carried out a thorough study of a *Ln*SbTe system, NdSbTe, by using angle-resolved photoemission spectroscopy along with first-principles calculations and thermodynamic measurements. We experimentally detect the presence of multiple gapless nodal-line states, which is well supported by first-principles calculations. A dispersive and an almost nondispersive nodal line exist along the bulk X-R direction. Another nodal line is present well below the Fermi level across the Γ-M direction, which is formed by bands with high Fermi velocity that seem to be sensitive to light polarization. Our study provides insight into the electronic structure of an alternative *Ln*SbTe material system that will aid towards understanding the connection of *Ln* elements with topological electronic structures in these systems.

I. INTRODUCTION

The experimental discovery of topological semimetal (TSM) phases has unleashed a flurry of research investigations in semimetallic quantum materials. The family of TSMs has since expanded to Dirac semimetals [1–3], Weyl semimetals [1,4–7], nodal-line semimetals [8–11], and beyond [12–15]. Different from the point degeneracy at the topological band crossings between the bulk valence and conduction bands in other classes of TSMs, the nodal-line semimetals feature band crossing that extends along a line or a loop [8]. Among the nodal-line semimetals, ZrSiS and similar 111 materials have been the most studied ones because of their ability to host multiple fermionic states including the nodal-line fermion and nonsymmorphic fermion originating from the square net of group-IV elements [10,11,16–23]. In addition to the topological fermions, these materials may also exhibit exotic properties including flat optical conductivity, unconventional magnetotransport, and unconventional mass enhancement [24–29].

Lanthanide (*Ln*)-based *Ln*SbTe systems belonging to the ZrSiS-type family of materials have recently become attractive to researchers because of (a) the Sb-square net, less studied compared to Si-square net materials, (b) possible magnetic ordering from the *Ln* magnetic moments, and (c) possible correlation effects brought by the $4f$ electrons of *Ln* elements. Despite these attractions, studies on the electronic structure of these *Ln*SbTe systems have been limited. One of the earlier works on one of such systems—antiferromagnetic (AFM) GdSbTe with a Néel temperature of about 12 K [30]—revealed a nodal-line state as well as an AFM Dirac state

protected by a combination of broken time-reversal symmetry and rotoinversion symmetry [31]. CeSbTe has been shown to be a potential ground for several topological features [32] and also a more symmetric nonsymmorphic Dirac state due to higher spin-orbit coupling (SOC) than ZrSiS [33]. While HoSbTe [34,35] and DySbTe [36] exhibit SOC gaps along all high-symmetry directions leading to a weak topological insulating state [36,37], LaSbTe features a gapless nodal line that persists even with SOC included [38]. Previous work on SmSbTe revealed multiple Dirac nodes that correspond to gapless nodal lines in this material system [39]. The presence of Dirac nodal lines in this system was also reported in another study, which also demonstrated the possibility of Kondo effects and electronic correlation enhancements [40]. These results demonstrate that the electronic structure of *Ln*SbTe depends on the choice of *Ln* element, however, a comprehensive understanding of how the electronic structure and topology in this family of materials evolve demands more electronic structure studies of *Ln*SbTe systems with different *Ln* elements. Out of such systems, NdSbTe has been reported to feature metamagnetic transitions and potentially a coexisting Kondo localization [41], which has been reported in CeSbTe as well [42–44]. Although transport and magnetic measurements have been performed in NdSbTe [41,45], the experimental measurement of the electronic structure is yet to be reported.

In this paper, we report a detailed study of NdSbTe through high-resolution angle-resolved photoemission spectroscopy (ARPES) measurements complemented by first-principles calculations and thermodynamic characterizations. Thermodynamic measurements show that NdSbTe is AFM with a transition temperature of around 2 K. Our experimental data in the paramagnetic phase show the presence of gapless nodal lines along multiple high-symmetry directions, in agreement
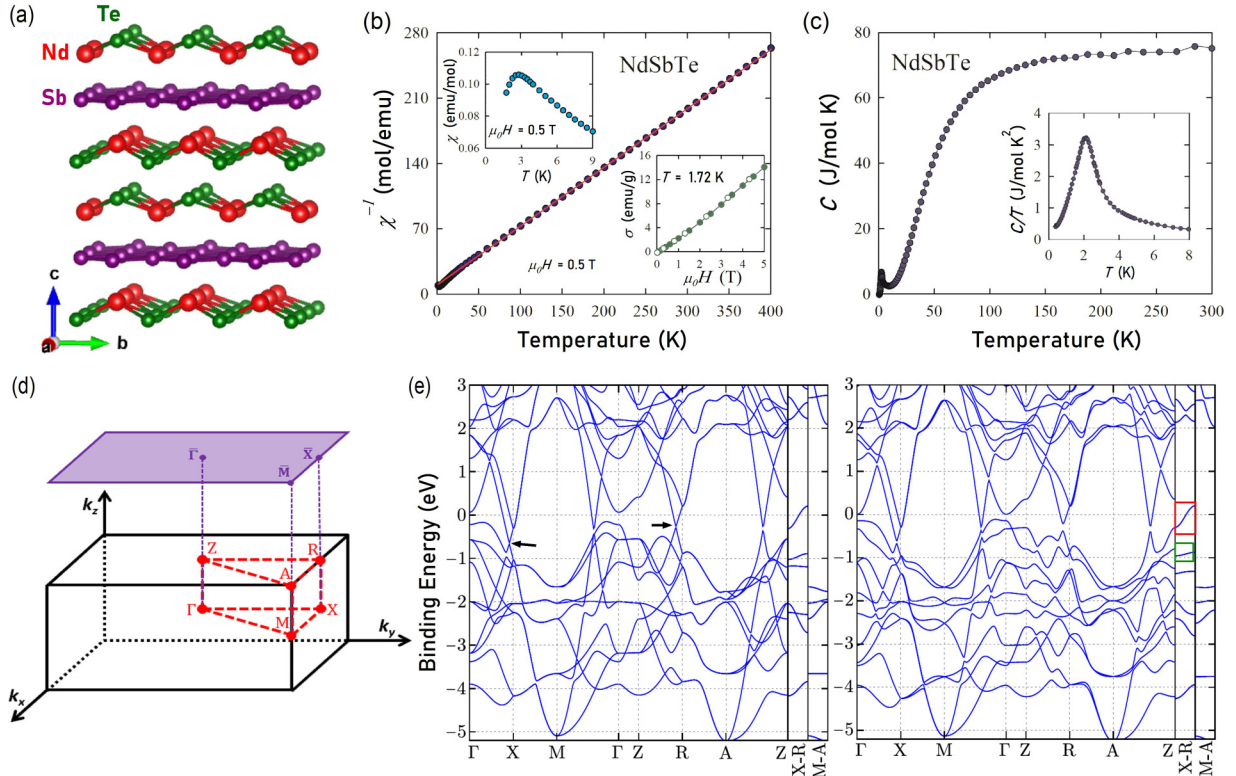
*Corresponding author: madhab.neupane@ucf.edu

FIG. 1. Bulk properties of NdSbTe. (a) Nonsymmorphic tetragonal crystal structure of NdSbTe. (b) Temperature dependence of the inverse magnetic susceptibility measured in a magnetic field of 0.5 T applied along the tetragonal axis. The solid red line represents the Curie-Weiss fit. Top left inset: Low-temperature magnetic susceptibility data. Bottom right inset: Magnetic field variation of the magnetization taken at 1.72 K with increasing (solid symbols) and decreasing (open symbols) field strength. The dashed line emphasizes a linear behavior below the metamagnetic transition. (c) Temperature variation of the specific heat. Inset: Low-temperature data plotted as the specific heat over temperature ratio vs temperature. (d) Bulk Brillouin zone and its projection onto a (001) surface Brillouin zone. High-symmetry points are marked. (e) Left: Calculated bulk bands along various high-symmetry directions without considering the spin-orbit coupling. Right: Calculated bulk bands with spin-orbit coupling taken into account.

with the predictions from the first-principles calculations. The bands associated with the nodal line around the Γ point across the Γ-M direction are observed to be sensitive to light polarization. A couple of nodal lines are observed along the X-R direction, with one in the vicinity of the Fermi level and the other residing around 800 meV below it. Overall, this study reveals the electronic structure and topological states in NdSbTe and presents a valuable platform towards having an understanding of the interplay of topology and Ln elements in the LnSbTe family of quantum materials.

II. METHODS

High-quality single crystals of NdSbTe were synthesized using the chemical vapor transport technique and characterized using energy-dispersive x-ray spectroscopy and single-crystal x-ray diffraction. Thermodynamic (heat capacity, magnetic susceptibility, magnetization) measurements were performed using commercial equipment. ARPES experiments were carried out at the Stanford Synchrotron Radiation Lightsource endstation 5-2 at a temperature of 18 K. The energy resolution of the ARPES analyzer was set to better than 20 meV. Density-functional theory [46,47] based first-principles calculations were carried out using the Vienna *ab initio* simulation package [48–50] on the basis of the

projector augmented-wave potential [51]. For more details, see Sec. 1 in the Supplemental Material (SM) [52].

III. RESULTS

A. Bulk properties of NdSbTe

The crystal structure of NdSbTe is presented in Fig. 1(a), where Nd-Te atomic layers sandwich the square nets formed by the Sb atoms. The structure is tetragonal in the nonsymmorphic space group No. 129 ($P4/nmm$). Figure 1(b) depicts the temperature dependence of the inverse magnetic susceptibility of NdSbTe measured in a magnetic field applied along the crystallographic c axis. Above 50 K, $\chi^{-1}(T)$ can be approximated by the Curie-Weiss (CW) law (note the solid straight line) with the effective magnetic moment $\mu_{\text{eff}} = 3.57(1)\mu_B$ and the paramagnetic Curie temperature $\theta_p = -17.4(2)$ K. The value of μ_{eff} is close to the theoretical Russell-Saunders prediction for a trivalent Nd ion ($3.62\mu_B$). The negative sign of θ_p signals AFM exchange interactions. Below 50 K, $\chi^{-1}(T)$ deviates from the CW behavior, likely due to the crystalline electric field (CEF) effect. As displayed in the top left inset of Fig. 1(b), $\chi(T)$ forms a maximum at $T_N = 2.7$ K that signals long-range AFM ordering. Another indication of the AFM character of the magnetically ordered state is the behavior of the magnetization measured
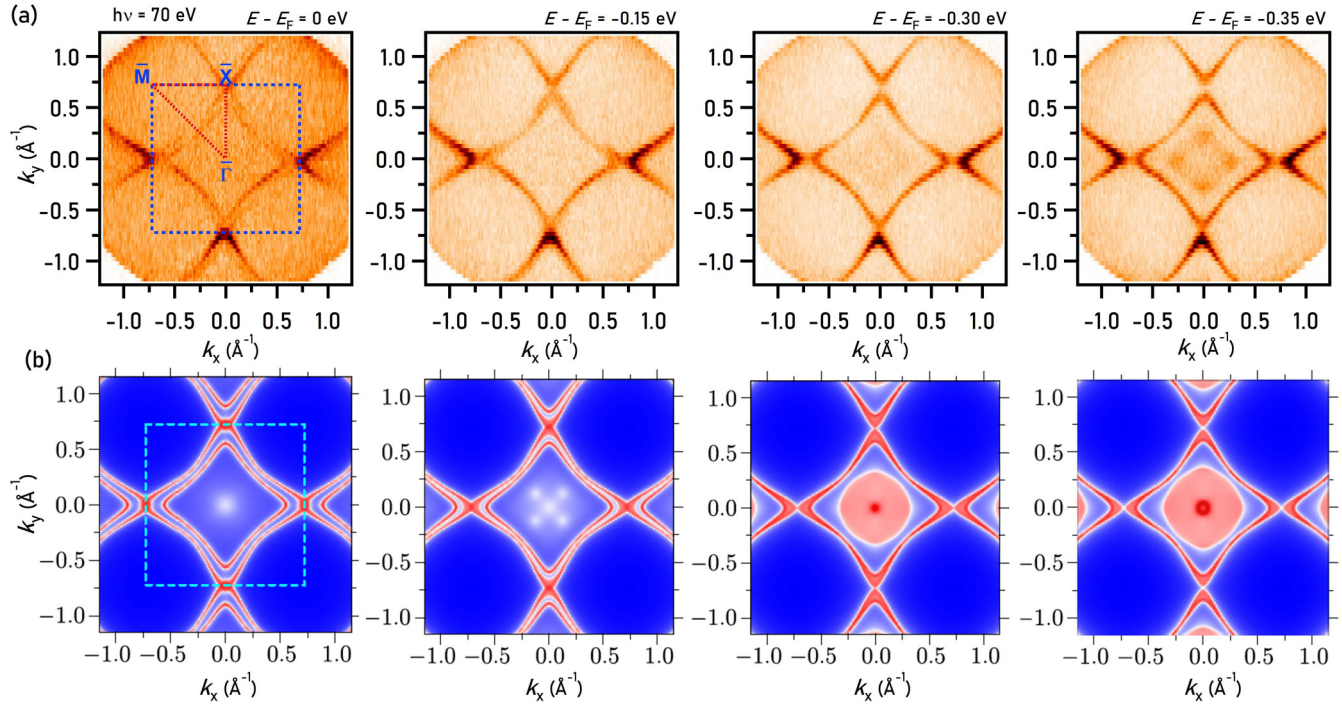
FIG. 2. FS and constant energy contours. (a) ARPES measured FS (first panel) and constant energy contours at various binding energies as noted on top of each plot. (b) Respective FS and energy contours obtained from first-principles calculations.

at $T = 1.72$ K as a function of magnetic field. As can be inferred from the lower inset to Fig. 1(b), $\sigma(H)$ is initially linear and exhibits a metamagneticlike transition near 2 T. In stronger fields, the magnetization shows a faint convex curvature and remains far from saturation. In a magnetic field of 5 T, the magnetization attains a value of 14.2(1) emu/g that corresponds to the magnetic moment of $1\mu_B$ that is much smaller than the theoretical prediction for the Nd^{3+} ion ($3.27\mu_B$). This reduction results mostly from the CEF interaction and single-ion anisotropy. The $\sigma(H)$ variation exhibits no hysteresis effect, in concert with the AFM nature of the magnetic ground state of NdSbTe. Figure 1(c) presents the temperature dependence of the specific heat of NdSbTe. Close to room temperature, $C(T)$ attains a value of about 74 J/(mol K) that is nearly equal to the Dulong-Petit limit [74.8 J/(mol K)]. With decreasing temperature, the specific heat decreases in a usual manner. The AFM phase transition manifests itself as a distinct mean-field-like anomaly in $C(T)$. As clearly seen in the inset to Fig. 1(c), the latter feature exhibits an extended tail above T_N that can be attributed to short-range exchange interactions. It is worth noting that overall the thermodynamic data collected for the single crystals of NdSbTe used in our ARPES study are very similar to the results obtained before by other research groups [41,45].

The lattice parameters of NdSbTe were theoretically optimized, and the so-obtained values $a = b = 4.371$ Å, and $c = 9.457$ Å are close to those reported before ($a = b = 4.312$ Å, and $c = 9.371$ Å [53]). The Wyckoff positions occupied by Nd, Sb, and Te atoms are, respectively, 2c (1/4, 1/4, 0.2769), 2a (3/4, 1/4, 0), and 2c (1/4, 1/4, 0.6279). In Fig. 1(d), we present the three-dimensional bulk Brillouin zone and its projection onto the two-dimensional (001) surface Brillouin zone. The high-symmetry points are marked on both the bulk

and surface Brillouin zones. The left and the right panels in Fig. 1(e) show the calculated bulk bands along different high-symmetry directions without and with the consideration of SOC, respectively. Dirac nodal lines are realized along the X-R and M-A directions (due to $P4/nmm$ symmetry). Within ± 1 eV of the Fermi level, the band structure without SOC shows Dirac nodes at the X and R points that correspond to nodal lines along the X-R direction. Dirac nodes are also present along Γ-X and Z-R [shown by black arrows in Fig. 1(e)]. However, when SOC is considered, these Dirac nodes along the Γ-X and Z-R directions gap out. These connect to the gapped nodal line along Γ-M (or Z-A) forming the diamondlike structure (see SM Fig. S2 for the exact bulk gap in the diamondlike structure [52]). The Dirac nodes at the X and R points remain gapless, leading to gapless nodal lines along X-R, even with SOC considered (also see Fig. S2 and Sec. 2 in the SM [52]). Specifically, the nodal line near the Fermi level (enclosed in the red rectangle) is dispersive with the Dirac node below the Fermi level at the X point, which moves upwards and above the Fermi level on reaching the R point. The other nodal line that lies slightly above -1 eV (enclosed in the green rectangle) shows very little dispersion along the X-R direction.

B. ARPES measured energy contours and surface state at the $\overline{X}$ point

Figures 2–5 present the results of the ARPES measurements on the NdSbTe single crystal. Note that the light source is linear horizontal (LH) polarized unless specified on top of the figure. The ARPES measured Fermi surface (FS) in Fig. 2(a) (first panel) is similar to the ZrSiS-type materials with a diamond-shaped pocket centered at the $\overline{\Gamma}$ point. The
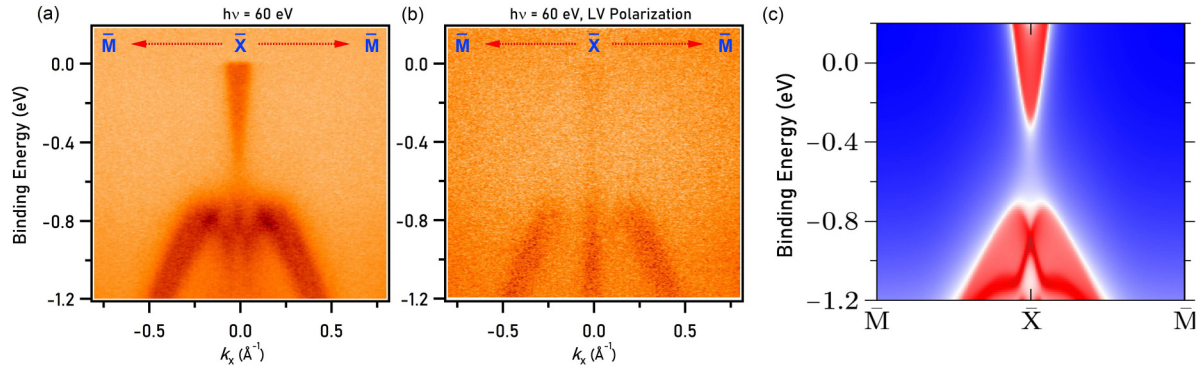
FIG. 3. Surface state along $\overline{M}$-$\overline{X}$-$\overline{M}$. (a), (b) Dispersion maps along $\overline{M}$-$\overline{X}$-$\overline{M}$ measured with linear horizontal and linear vertical polarized light with energy 60 eV, respectively. (c) Calculated surface spectrum along $\overline{M}$-$\overline{X}$-$\overline{M}$.

diamond pocket has double sheets, out of which the inner sheet is strongly visible and the outer one has a very faint intensity. The double sheet nature of the FS is well reproduced in the calculated FS [Fig. 2(b), first panel]. The sheet separation in the momentum space reduces with increasing binding energy and finally turns into a single sheet at higher values of binding energies, as seen in the constant energy contours at 300 meV binding energy, where a new pocket emerges at the center of the Brillouin zone. Several bulk pockets appear at higher binding energies, which can be clearly visualized from the constant energy contour plots at binding energies of 350,

500, and 700 meV (see Sec. 2 in the SM [52]). The calculated energy contours well reproduce the experimental ones. The exception of the intense circular pocket at the higher binding energy can be explained from the polarization dependence, which can be seen from the polarization-dependent maps presented in Sec. 3 of the SM [52].

In order to understand the underlying electronic structure of NdSbTe at low temperatures, we analyze the dispersion maps along various high-symmetry directions in Figs. 3–5. We begin with the dispersion maps along the $\overline{M}$-$\overline{X}$-$\overline{M}$, which is presented in Fig. 3. A gapped Dirac-like state is observed at
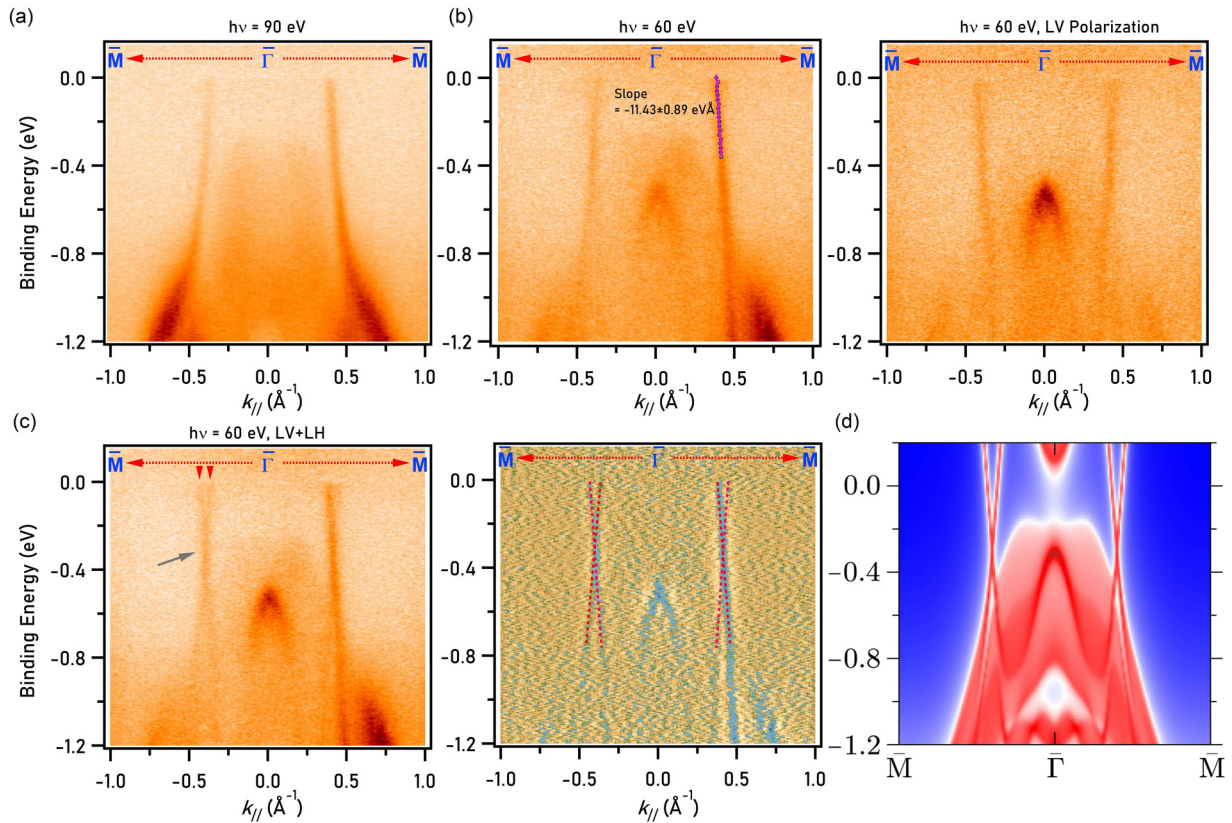
FIG. 4. Band dispersion along $\overline{M}$-$\overline{\Gamma}$-$\overline{M}$. (a), (b) Dispersion maps along the $\overline{M}$-$\overline{\Gamma}$-$\overline{M}$ direction measured at photon energies of 90 and 60 eV, respectively. The left panel in (b) shows the dispersion map measured with linear vertical polarization. (c) Dispersion map at 60 eV photon energy with both linear horizontal and liner vertical data added. The right panel shows the second derivative plot of the dispersion map in the left panel. (d) Calculated surface band spectrum along $\overline{M}$-$\overline{\Gamma}$-$\overline{M}$.
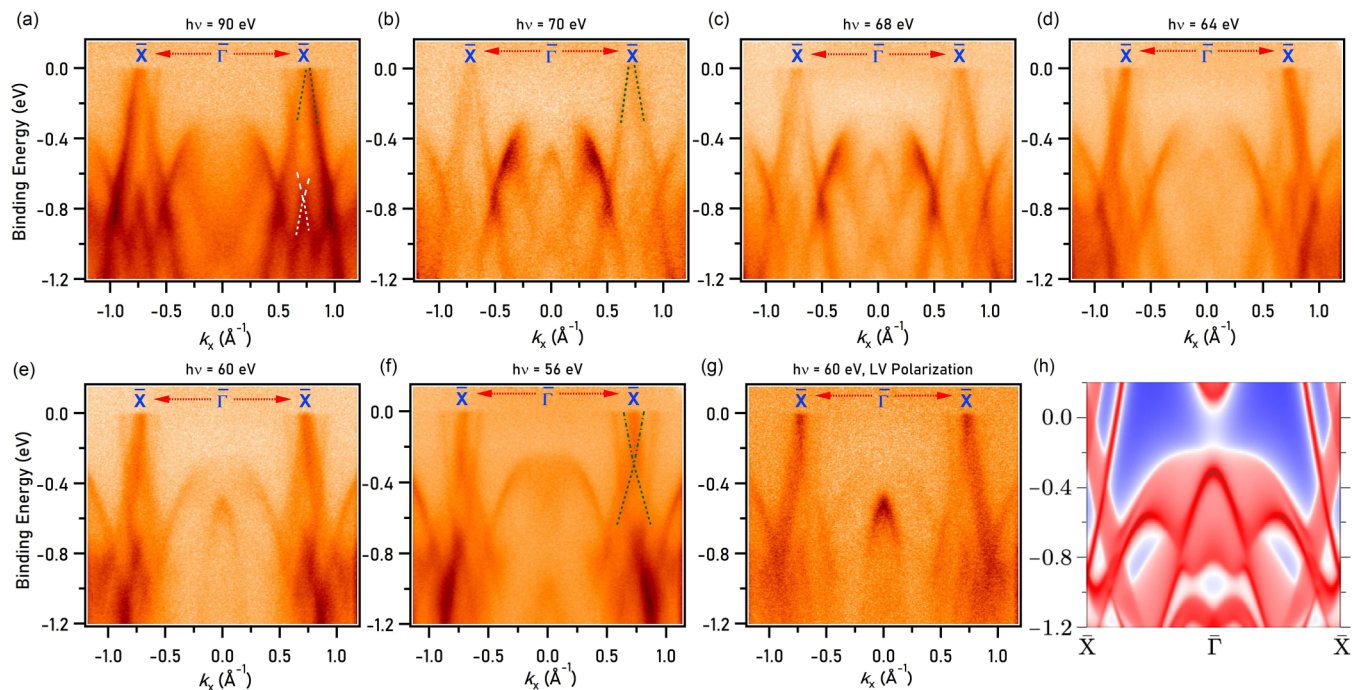
FIG. 5. Band dispersion along $\overline{X}$-$\overline{\Gamma}$-$\overline{X}$. (a) Dispersion map along the $\overline{X}$-$\overline{\Gamma}$-$\overline{X}$ direction measured with different photon energy of 90 eV. (b) Photon energy-dependent dispersion maps along $\overline{X}$-$\overline{\Gamma}$-$\overline{X}$ with the value of photon energy noted on top of each plot. (c) $\overline{X}$-$\overline{\Gamma}$-$\overline{X}$ band structure measured with a 60 eV linear vertical polarized photon source. (d) Calculated surface projected band structure along the $\overline{X}$-$\overline{\Gamma}$-$\overline{X}$ direction.

the $\overline{X}$ point. The dispersion of this state does not seem to depend on the choice of photon energy (see Sec. 5 in the SM [52] for more photon energy measurements), which implies that this state is surface originated. The surface state coexists with bulk states (see the slab calculation in SM Sec. 4 [52]). As seen in Fig. 3(a), the surface state is strong in measurement with the LH polarized photon source and strongly suppressed in measurement with the linear vertical (LV) polarized light source [Fig. 3(b)]. The calculated surface spectrum is presented in Fig. 3(c), which fairly reproduces the experimental observation of the gapped surface state at the $\overline{X}$ point.

C. Observation of gapless nodal-line states

Next, we move on to the experimental electronic band dispersion along the $\overline{M}$-$\overline{\Gamma}$-$\overline{M}$ direction. Figure 4(a) represents a dispersion map measured with a photon energy of 90 eV along this direction. A single band can be seen crossing the Fermi level. A similar band dispersion is observed in the measurement carried out with 60 eV photon energy [Fig. 4(b), left panel]. This band has an almost linear dispersion up to ~0.8 eV below the Fermi level and is slightly converging towards the $\overline{\Gamma}$ point. The Fermi velocity is very large [11.43 ± 0.89 eV Å as obtained from the slope of the linear fit of peaks in the momentum distribution curves within -360 meV binding energy; see Fig. 4(b), left panel] compared to the $\overline{\Gamma}$-$\overline{M}$ bands in ZrSiS [54]. The observation of a double sheet FS means that there should be two bands crossing the Fermi level along this direction. A strong suppression of the outer sheet in the FS map and the observation of a single band extending up to the Fermi level along $\overline{M}$-$\overline{\Gamma}$-$\overline{M}$ in the measurements with LH polarization pointed to the possibility of polarization dependence of the outer band. We therefore

performed a measurement with LV polarized light [Fig. 4(b), right panel], where we again observed a single band crossing the Fermi level. This band is also almost linear above -500 meV. Interestingly, unlike the band observed in LH polarization, this band seems to slightly diverge away from the $\overline{\Gamma}$ point. In Fig. 4(c), we present the dispersion map along $\overline{M}$-$\overline{\Gamma}$-$\overline{M}$ with the LH and LV polarization matrices added. We can clearly observe two bands crossing the Fermi level, out of which the inner one is sensitive to LH polarization and the outer one is sensitive to LV polarization (also see Sec. 3 in the SM [52]). This explains the double sheet nature of the diamond pocket in the Fermi surface. These two bands cross each other at around 300 meV below the Fermi level and disperse almost linearly across this crossing point, giving an impression of a gapless nodal line along the $\overline{\Gamma}$-$\overline{M}$ direction. This can be clearly visualized in the second derivative plot presented in Fig. 4(c) (right panel), where the crossing between the bands is shown by two red-colored dashed lines. The calculated band structure along this direction is presented in Fig. 4(d), which clearly shows this crossing feature. Despite the experimental observation of the gapless nodal line in experiments, it is important to note that the bulk calculation shows a gapped nature along this direction [Fig. 1(d)] and the calculation in Fig. 4(d) is integrated for all values of k_z. The k_z plane-dependent bulk bands presented in Sec. 6 of the SM [52] also show a gapped nature for any particular value of k_z, which is undetectable in ARPES data. Such a nodal line with an undetectable gap within the experimental resolution was reported in a similar LnSbTe-type material [40]. The ARPES measurement in the vacuum ultraviolet region has poor k_z resolution and hence the data observed in the experiments probably cover a certain range of k_z value rather than a certain k_z plane. The other possibility could be because

of the discrepancy between experimental data and theoretical calculations that is usual for metallic/semimetallic systems.

In Fig. 5, we present the dispersion maps along the $\overline{X}$-$\overline{\Gamma}$-$\overline{X}$ direction. The measured dispersion map along this direction with a photon energy of 90 eV [Fig. 5(a)] shows a linearly dispersing band (green dashed line) crossing the Fermi level around the $\overline{X}$ point. In addition, another linear band touching is present at the $\overline{X}$ point about 760 meV below the Fermi level. In Figs. 5(b)–5(f), $\overline{X}$-$\overline{\Gamma}$-$\overline{X}$ band dispersions measured with different photon energies are presented. The linear dispersion in the vicinity of the Fermi level seems to be strongly photon energy dependent. This photon energy dependence is indicative of the bulk origination of the bands associated with the linear dispersion. The crossing point of the linear dispersion lies well below the Fermi level at a photon energy of 56 eV [$k_z \sim 0$, Fig. 5(f)] and it shifts upwards and above the Fermi level on increasing the photon energy up to 70 eV [$k_z \sim \pi$, Fig. 5(b)]. This agrees well with the theoretical prediction of the dispersive and gapless nodal line along the X-R direction. The presence of a gapless nodal line in the vicinity of the Fermi level has been recently reported in similar compounds SmSbTe [39] and LaSbTe [38]. The band-touching feature around 760 meV, on the other hand, seems to have very little change with photon energy variation, in agreement with the almost dispersionless and gapless nodal line along the X-R direction as seen in the bulk-band calculations. This feature is also observed to be sensitive to LH polarization and is strongly suppressed when the incident photon is LV polarized [see Fig. 5(g)]. The observation of the Dirac nodes along the $\overline{X}$-$\overline{\Gamma}$-$\overline{X}$ direction is well reproduced in the calculated surface electronic structure shown in Fig. 5(h) (also see Sec. 6 in the SM [52]).

IV. CONCLUSION

In summary, through high-resolution ARPES measurements supported by theoretical calculations, we studied the detailed low-temperature electronic structure in the *Ln*-based ZrSiS-type material NdSbTe. The thermodynamic measurements indicated an AFM transition in this material with a Néel temperature $T_N \sim 2$ K. Our ARPES results in the paramagnetic phase detect three gapless nodal lines in this material system—two along the bulk X-R direction and one around the Γ point formed by steep bands with a high Fermi velocity that constitute the diamond shape. Although theory predicts that the nodal line around the Γ point is gapped, experimental results show a gapless feature. The theoretical calculations well reproduce the experimental results. This work presents NdSbTe as a multiple nodal-line fermion system and provides an alternative platform to understand the evolution of the topology and electronic structure among the *Ln*SbTe family of materials.

[1] N. P. Armitage, E. J. Mele, and A. Vishwanath, Weyl and Dirac semimetals in three-dimensional solids, Rev. Mod. Phys. **90**, 015001 (2018).

[2] Z. K. Liu, B. Zhou, Y. Zhang, Z. J. Wang, H. M. Weng, D. Prabhakaran, S. K. Mo, Z. X. Shen, Z. Fang, X. Dai, Z. Hussain, and Y. L. Chen, Discovery of a three-dimensional topological Dirac semimetal, Na₃Bi, Science **343**, 864 (2014).

[3] M. Neupane, S.-Y. Xu, R. Sankar, N. Alidoust, G. Bian, C. Liu, I. Belopolski, T.-R. Chang, H.-T. Jeng, H. Lin, A. Bansil, F. Chou, and M. Z. Hasan, Observation of a three-dimensional topological Dirac semimetal phase in high-mobility Cd₃As₂, Nat. Commun. **5**, 3786 (2014).

[4] S.-Y. Xu, I. Belopolski, N. Alidoust, M. Neupane, G. Bian, C. Zhang, R. Sankar, G. Chang, Z. Yuan, C.-C. Lee, S.-M. Huang, H. Zheng, J. Ma, D. S. Sanchez, B. Wang, A. Bansil, F. Chou, P. P. Shibayev, H. Lin, S. Jia *et al.*, Discovery of a Weyl fermion semimetal and topological Fermi arcs, Science **349**, 613 (2015).

[5] B. Q. Lv, H. M. Weng, B. B. Fu, X. P. Wang, H. Miao, J. Ma, P. Richard, X. C. Huang, L. X. Zhao, G. F. Chen, Z. Fang, X. Dai, T. Qian, and H. Ding, Experimental Discovery of Weyl Semimetal TaAs, Phys. Rev. X **5**, 031013 (2015).

[6] B. Yan and C. Felser, Topological materials: Weyl semimetals, Annu. Rev. Condens. Matter Phys. **8**, 337 (2017).

[7] A. A. Soluyanov, D. Gresch, Z. Wang, Q. Wu, M. Troyer, X. Dai, and B. A. Bernevig, Type-II Weyl semimetals, Nature (London) **527**, 495 (2015).

[8] A. A. Burkov, M. D. Hook, and L. Balents, Topological nodal semimetals, Phys. Rev. B **84**, 235126 (2011).

[9] G. Bian, T.-R. Chang, R. Sankar, S.-Y. Xu, H. Zheng, T. Neupert, C.-K. Chiu, S.-M. Huang, G. Chang, I. Belopolski, D. S. Sanchez, M. Neupane, N. Alidoust, C. Liu, B. Wang, C.-C. Lee, H.-T. Jeng, C. Zhang, Z. Yuan, S. Jia *et al.*, Topological nodal-line fermions in spin-orbit metal PbTaSe₂, Nat. Commun. **7**, 10556 (2016).

[10] M. Neupane, I. Belopolski, M. M. Hosen, D. S. Sanchez, R. Sankar, M. Szlawska, S.-Y. Xu, K. Dimitri, N. Dhakal, P. Maldonado, P. M. Oppeneer, D. Kaczorowski, F. Chou, M. Z. Hasan, and T. Durakiewicz, Observation of topological nodal fermion semimetal phase in ZrSiS, Phys. Rev. B **93**, 201104(R) (2016).

[11] L. M. Schoop, M. N. Ali, C. Straßer, A. Topp, A. Varykhalov, D. Marchenko, V. Duppel, S. S. P. Parkin, B. V. Lotsch, and C. R. Ast, Dirac cone protected by non-symmorphic symmetry

and three-dimensional Dirac line node in ZrSiS, Nat. Commun. **7**, 11696 (2016).

[12] B. Bradlyn, J. Cano, Z. Wang, M. G. Vergniory, C. Felser, R. J. Cava, and B. A. Bernevig, Beyond Dirac and Weyl fermions: Unconventional quasiparticles in conventional crystals, Science **353**, aaf5037 (2016).

[13] D. Takane, Z. Wang, S. Souma, K. Nakayama, T. Nakamura, H. Oinuma, Y. Nakata, H. Iwasawa, C. Cacho, T. Kim, K. Horiba, H. Kumigashira, T. Takahashi, Y. Ando, and T. Sato, Observation of Chiral Fermions with a Large Topological Charge and Associated Fermi-Arc Surface States in CoSi, Phys. Rev. Lett. **122**, 076402 (2019).

[14] D. S. Sanchez, I. Belopolski, T. A. Cochran, X. Xu, J.-X. Yin, G. Chang, W. Xie, K. Manna, V. Süß, C.-Y. Huang, N. Alidoust, D. Multer, S. S. Zhang, N. Shumiya, X. Wang, G.-Q. Wang, T.-R. Chang, C. Felser, S.-Y. Xu, S. Jia, H. Lin *et al.*, Topological chiral crystals with helicoid-arc quantum states, Nature (London) **567**, 500 (2019).

[15] I. Belopolski, K. Manna, D. S. Sanchez, G. Chang, B. Ernst, J. Yin, S. S. Zhang, T. Cochran, N. Shumiya, H. Zheng, B. Singh, G. Bian, D. Multer, M. Litskevich, X. Zhou, S.-M. Huang, B. Wang, T.-R. Chang, S.-Y. Xu, A. Bansil *et al.*, Discovery of topological Weyl fermion lines and drumhead surface states in a room temperature magnet, Science **365**, 1278 (2019).

[16] A. Topp, J. M. Lippmann, A. Varykhalov, V. Duppel, B. V. Lotsch, C. R. Ast, and L. M. Schoop, Non-symmorphic band degeneracy at the Fermi level in ZrSiTe, New J. Phys. **18**, 125014 (2016).

[17] J. Hu, Z. Tang, J. Liu, X. Liu, Y. Zhu, D. Graf, K. Myhro, S. Tran, C. N. Lau, J. Wei, and Z. Mao, Evidence of Topological Nodal-Line Fermions in ZrSiSe and ZrSiTe, Phys. Rev. Lett. **117**, 016602 (2016).

[18] D. Takane, Z. Wang, S. Souma, K. Nakayama, C. X. Trang, T. Sato, T. Takahashi, and Y. Ando, Dirac-node arc in the topological line-node semimetal HfSiS, Phys. Rev. B **94**, 121108(R) (2016).

[19] M. M. Hosen, K. Dimitri, I. Belopolski, P. Maldonado, R. Sankar, N. Dhakal, G. Dhakal, T. Cole, P. M. Oppeneer, D. Kaczorowski, F. Chou, M. Z. Hasan, T. Durakiewicz, and M. Neupane, Tunability of the topological nodal-line semimetal phase in ZrSi*X*-type materials (*X* = S, Se, Te), Phys. Rev. B **95**, 161101(R) (2017).

[20] C. Chen, X. Xu, J. Jiang, S. C. Wu, Y. P. Qi, L. X. Yang, M. X. Wang, Y. Sun, N. B. M. Schröter, H. F. Yang, L. M. Schoop, Y. Y. Lv, J. Zhou, Y. B. Chen, S. H. Yao, M. H. Lu, Y. F. Chen, C. Felser, B. H. Yan, Z. K. Liu, and Y. L. Chen, Dirac line nodes and effect of spin-orbit coupling in the nonsymmorphic critical semimetals *M*SiS(*M* = Hf, Zr), Phys. Rev. B **95**, 125126 (2017).

[21] R. Lou, J. Z. Ma, Q. N. Xu, B. B. Fu, L. Y. Kong, Y. G. Shi, P. Richard, H. M. Weng, Z. Fang, S. S. Sun, Q. Wang, H. C. Lei, T. Qian, H. Ding, and S. C. Wang, Emergence of topological bands on the surface of ZrSnTe crystal, Phys. Rev. B **93**, 241104(R) (2016).

[22] M. M. Hosen, K. Dimitri, A. Aperis, P. Maldonado, I. Belopolski, G. Dhakal, F. Kabir, C. Sims, M. Z. Hasan, D. Kaczorowski, T. Durakiewicz, P. M. Oppeneer, and M. Neupane, Observation of gapless Dirac surface states in ZrGeTe, Phys. Rev. B **97**, 121103(R) (2018).

[23] B. B. Fu, C. J. Yi, T. T. Zhang, M. Caputo, J. Z. Ma, X. Gao, B. Q. Lv, L. Y. Kong, Y. B. Huang, P. Richard, M. Shi, V. N. Strocov, C. Fang, H. M. Weng, Y. G. Shi, T. Qian, and H. Ding, Dirac nodal surfaces and nodal lines in ZrSiS, Sci. Adv. **5**, eaau6459 (2019).

[24] M. N. Ali, L. M. Schoop, C. Garg, J. M. Lippmann, E. Lara, B. Lotsch, and S. S. P. Parkin, Butterfly magnetoresistance, quasi-2D Dirac Fermi surface and topological phase transition in ZrSiS, Sci. Adv. **2**, e1601742 (2016).

[25] Y.-Y. Lv, B.-B. Zhang, X. Li, S.-H. Yao, Y. B. Chen, J. Zhou, S.-T. Zhang, M.-H. Lu, and Y.-F. Chen, Extremely large and significantly anisotropic magnetoresistance in ZrSiS single crystals, Appl. Phys. Lett. **108**, 244101 (2016).

[26] M. B. Schilling, L. M. Schoop, B. V. Lotsch, M. Dressel, and A. V. Pronin, Flat Optical Conductivity in ZrSiS due to Two-Dimensional Dirac Bands, Phys. Rev. Lett. **119**, 187401 (2017).

[27] R. Singha, A. K. Pariari, B. Satpati, and P. Mandal, Large non-saturating magnetoresistance and signature of nondegenerate Dirac nodes in ZrSiS, Proc. Natl. Acad. Sci. USA **114**, 2468 (2017).

[28] N. Kumar, K. Manna, Y. Qi, S.-C. Wu, L. Wang, B. Yan, C. Felser, and C. Shekhar, Unusual magnetotransport from Si-square nets in topological semimetal HfSiS, Phys. Rev. B **95**, 121109(R) (2017).

[29] S. Pezzini, M. R. van Delft, L. M. Schoop, B. V. Lotsch, A. Carrington, M. I. Katsnelson, N. E. Hussey, and S. Wiedmann, Unconventional mass enhancement around the Dirac nodal loop in ZrSiS, Nat. Phys. **14**, 178 (2018).

[30] R. Sankar, I. P. Muthuselvam, K. R. Babu, G. S. Murugan, K. Rajagopal, R. Kumar, T.-C. Wu, C.-Y. Wen, W.-L. Lee, G.-Y. Guo, and F.-C. Chou, Crystal growth and magnetic properties of topological nodal-line semimetal GdSbTe with antiferromagnetic spin ordering, Inorg. Chem. **58**, 11730 (2019).

[31] M. M. Hosen, G. Dhakal, K. Dimitri, P. Maldonado, A. Aperis, F. Kabir, C. Sims, P. Riseborough, P. M. Oppeneer, D. Kaczorowski, T. Durakiewicz, and M. Neupane, Discovery of topological nodal-line fermionic phase in a magnetic material GdSbTe, Sci. Rep. **8**, 13283 (2018).

[32] L. M. Schoop, A. Topp, J. Lippmann, F. Orlandi, L. Müchler, M. G. Vergniory, Y. Sun, A. W. Rost, V. Duppel, M. Krivenkov, S. Sheoran, P. Manuel, A. Varykhalov, B. Yan, R. K. Kremer, C. R. Ast, and B. V. Lotsch, Tunable Weyl and Dirac states in the nonsymmorphic compound CeSbTe, Sci. Adv. **4**, eaar2317 (2018).

[33] A. Topp, M. G. Vergniory, M. Krivenkov, A. Varykhalov, F. Rodolakis, J. L. McChesney, B. V. Lotsch, C. R. Ast, and L. M. Schoop, The effect of spin-orbit coupling on nonsymmorphic square-net compounds, J. Phys. Chem. Solids **128**, 296 (2019).

[34] S. Yue, Y. Qian, M. Yang, D. Geng, C. Yi, S. Kumar, K. Shimada, P. Cheng, L. Chen, Z. Wang, H. Weng, Y. Shi, K. Wu, and B. Feng, Topological electronic structure in the antiferromagnet HoSbTe, Phys. Rev. B **102**, 155109 (2020).

[35] M. Yang, Y. Qian, D. Yan, Y. Li, Y. Song, Z. Wang, C. Yi, H. L. Feng, H. Weng, and Y. Shi, Magnetic and electronic properties of a topological nodal line semimetal candidate: HoSbTe, Phys. Rev. Mater. **4**, 094203 (2020).

[36] F. Gao, J. Huang, W. Ren, M. Li, H. Wang, T. Yang, B. Li, and Z. Zhang, Magnetic and transport properties of the topological compound DySbTe, Phys. Rev. B **105**, 214434 (2022).

[37] N. Shumiya, J.-X. Yin, G. Chang, M. Yang, S. Mardanya, T.-R. Chang, H. Lin, M. S. Hossain, Y.-X. Jiang, T. A. Cochran, Q. Zhang, X. P. Yang, Y. Shi, and M. Z. Hasan, Evidence for electronic signature of a magnetic transition in the topological magnet HoSbTe, Phys. Rev. B **106**, 035151 (2022).

[38] Y. Wang, Y. Qian, M. Yang, H. Chen, C. Li, Z. Tan, Y. Cai, W. Zhao, S. Gao, Y. Feng, S. Kumar, E. F. Schwier, L. Zhao, H. Weng, Y. Shi, G. Wang, Y. Song, Y. Huang, K. Shimada, Z. Xu *et al.*, Spectroscopic evidence for the realization of a genuine topological nodal-line semimetal in LaSbTe, Phys. Rev. B **103**, 125131 (2021).

[39] S. Regmi, G. Dhakal, F. C. Kabeer, N. Harrison, F. Kabir, A. P. Sakhya, K. Gofryk, D. Kaczorowski, P. M. Oppeneer, and M. Neupane, Observation of multiple nodal lines in SmSbTe, Phys. Rev. Mater. **6**, L031201 (2022).

[40] K. Pandey, D. Mondal, J. W. Villanova, J. Roll, R. Basnet, A. Wegner, G. Acharya, M. R. U. Nabi, B. Ghosh, J. Fujii, J. Wang, B. Da, A. Agarwal, I. Vobornik, A. Politano, S. Barraza-Lopez, and J. Hu, Magnetic topological semimetal phase with electronic correlation enhancement in SmSbTe, Adv. Quantum Technol. **4**, 2100063 (2021).

[41] K. Pandey, R. Basnet, A. Wegner, G. Acharya, M. R. U. Nabi, J. Liu, J. Wang, Y. K. Takahashi, B. Da, and J. Hu, Electronic and magnetic properties of the topological semimetal candidate NdSbTe, Phys. Rev. B **101**, 235161 (2020).

[42] K. W. Chen, Y. Lai, Y. C. Chiu, S. Steven, T. Besara, D. Graf, T. Siegrist, T. E. Albrecht-Schmitt, L. Balicas, and R. E. Baumbach, Possible devil's staircase in the Kondo lattice CeSbTe, Phys. Rev. B **96**, 014421 (2017).

[43] B. Lv, J. Chen, L. Qiao, J. Ma, X. Yang, M. Li, M. Wang, Q. Tao, and Z.-A. Xu, Magnetic and transport properties of low-carrier-density Kondo semimetal CeSbTe, J. Phys.: Condens. Matter **31**, 355601 (2019).

[44] P. Li, B. Lv, Y. Fang, W. Guo, Z. Wu, Y. Wu, D. Shen, Y. Nie, L. Petaccia, C. Cao, Z.-A. Xu, and Y. Liu, Charge density wave and weak Kondo effect in a Dirac semimetal CeSbTe, Sci. China: Phys. Mech. Astron. **64**, 237412 (2021).

[45] R. Sankar, I. P. Muthuselvam, K. Rajagopal, K. Ramesh Babu, G. S. Murugan, K. S. Bayikadi, K. Moovendaran, C. T. Wu, and G.-Y. Guo, Anisotropic magnetic properties of nonsymmorphic semimetallic single crystal NdSbTe, Cryst. Growth Des. **20**, 6585 (2020).

[46] P. Hohenberg and W. Kohn, Inhomogeneous electron gas, Phys. Rev. **136**, B864 (1964).

[47] W. Kohn and L. J. Sham, Self-Consistent Equations Including Exchange and Correlation Effects, Phys. Rev. **140**, A1133 (1965).

[48] G. Kresse and J. Hafner, *Ab initio* molecular-dynamics simulation of the liquid-metal–amorphous-semiconductor transition in germanium, Phys. Rev. B **49**, 14251 (1994).

[49] G. Kresse and J. Furthmüller, Efficient iterative schemes for *ab initio* total-energy calculations using a plane-wave basis set, Phys. Rev. B **54**, 11169 (1996).

[50] G. Kresse and D. Joubert, From ultrasoft pseudopotentials to the projector augmented-wave method, Phys. Rev. B **59**, 1758 (1999).

[51] P. E. Blöchl, Projector augmented-wave method, Phys. Rev. B **50**, 17953 (1994).

[52] See Supplemental Material at http://link.aps.org/supplemental/10.1103/PhysRevMaterials.7.044202 for details on the methods

and additional experimental and theoretical results, which includes Refs. [30,41,45–51,55–71].

[53] J. P. Charvillat, D. Damien, and A. Wojakowski, Crystal chemistry of binary MSb_2 and ternary $MSbTe$ compounds of transuranium elements, Rev. Chim. Miner. **14**, 178 (1977).

[54] M. S. Lodge, G. Chang, C.-Y. Huang, B. Singh, J. Hellerstedt, M. T. Edmonds, D. Kaczorowski, M. M. Hosen, M. Neupane, H. Lin, M. S. Fuhrer, B. Weber, and M. Ishigami, Observation of effective pseudospin scattering in ZrSiS, Nano Lett. **17**, 7213 (2017).

[55] J. P. Perdew, K. Burke, and M. Ernzerhof, Generalized Gradient Approximation Made Simple, Phys. Rev. Lett. **77**, 3865 (1996).

[56] H. J. Monkhorst and J. D. Pack, Special points for Brillouin-zone integrations, Phys. Rev. B **13**, 5188 (1976).

[57] K. Pandey, R. Basnet, J. Wang, B. Da, and J. Hu, Evolution of electronic and magnetic properties in the topological semimetal $SmSb_xTe_{2-x}$, Phys. Rev. B **105**, 155139 (2022).

[58] I. Plokhikh, V. Pomjakushin, D. J. Gawryluk, O. Zaharko, and E. Pomjakushina, Competing magnetic phases in $LnSbTe$ (Ln = Ho and Tb), Inorg. Chem. **61**, 11399 (2022).

[59] A. I. Liechtenstein, V. I. Anisimov, and J. Zaanen, Density-functional theory and strong interactions: Orbital ordering in Mott-Hubbard insulators, Phys. Rev. B **52**, R5467 (1995).

[60] P. Giannozzi, S. Baroni, N. Bonini, M. Calandra, R. Car, C. Cavazzoni, D. Ceresoli, G. L. Chiarotti, M. Cococcioni, I. Dabo, A. Dal Corso, S. de Gironcoli, S. Fabris, G. Fratesi, R. Gebauer, U. Gerstmann, C. Gougoussis, A. Kokalj, M. Lazzeri, L. Martin-Samos, N. Marzari *et al.*, QUANTUM ESPRESSO: A modular and open-source software project for quantum simulations of materials, J. Phys.: Condens. Matter **21**, 395502 (2009).

[61] P Giannozzi, O. Andreussi, T. Brumme, O. Bunau, M. Buongiorno Nardelli, M. Calandra, R. Car, C. Cavazzoni, D. Ceresoli, M. Cococcioni, N. Colonna, I. Carnimeo, A. Dal Corso, S. de Gironcoli, P. Delugas, R. A. DiStasio, A. Ferretti, A. Floris, G. Fratesi, G. Fugallo *et al.*, Advanced capabilities for materials modelling with Quantum ESPRESSO, J. Phys.: Condens. Matter **29**, 465901 (2017).

[62] P. Giannozzi, O. Baseggio, P. Bonfá, D. Brunato, R. Car, I. Carnimeo, C. Cavazzoni, S. de Gironcoli, P. Delugas, F. Ferrari Ruffino, A. Ferretti, N. Marzari, I. Timrov, A. Urru, and S. Baroni, Quantum ESPRESSO toward the exascale, J. Chem. Phys. **152**, 154105 (2020).

[63] A. Dal Corso, Pseudopotentials periodic table: From H to Pu, Comput. Mater. Sci. **95**, 337 (2014).

[64] N. Marzari, A. A. Mostofi, J. R. Yates, I. Souza, and D. Vanderbilt, Maximally localized Wannier functions: Theory and applications, Rev. Mod. Phys. **84**, 1419 (2012).

[65] N. Marzari and D. Vanderbilt, Maximally localized generalized Wannier functions for composite energy bands, Phys. Rev. B **56**, 12847 (1997).

[66] I. Souza, N. Marzari, and D. Vanderbilt, Maximally localized Wannier functions for entangled energy bands, Phys. Rev. B **65**, 035109 (2001).

[67] A. A. Mostofi, J. R. Yates, Y.-S. Lee, I. Souza, D. Vanderbilt, and N. Marzari, Wannier90: A tool for obtaining maximally-localised Wannier functions, Comput. Phys. Commun. **178**, 685 (2008).

[68] A. A. Mostofi, J. R. Yates, G. Pizzi, Y.-S. Lee, I. Souza, D. Vanderbilt, and N. Marzari, An updated version of wannier90: A tool for obtaining maximally-localised Wannier functions, Comput. Phys. Commun. **185**, 2309 (2014).

[69] G. Pizzi, V. Vitale, R. Arita, S. Blügel, F. Freimuth, G. Géranton, M. Gibertini, D. Gresch, C. Johnson, T. Koretsune, J. Ibañez-Azpiroz, H. Lee, J.-M. Lihm, D. Marchand, A. Marrazzo, Y. Mokrousov, J. I. Mustafa, Y. Nohara, Y. Nomura, L. Paulatto, S. Poncé, T. Ponweiser, J. Qiao, F. Thöle, S. S. Tsirkin *et al.*, Wannier90 as a community code: new fea-tures and applications, J. Phys.: Condens. Matter **32**, 165902 (2020).

[70] M. P. L. Sancho, J. M. L. Sancho, J. M. L. Sancho, and J. Rubio, Highly convergent schemes for the calculation of bulk and surface Green functions, J. Phys. F: Met. Phys. **15**, 851 (1985).

[71] Q. Wu, S. Zhang, H.-F. Song, M. Troyer, and A. A. Soluyanov, WannierTools: An open-source software package for novel topological materials, Comput. Phys. Commun. **224**, 405 (2018).